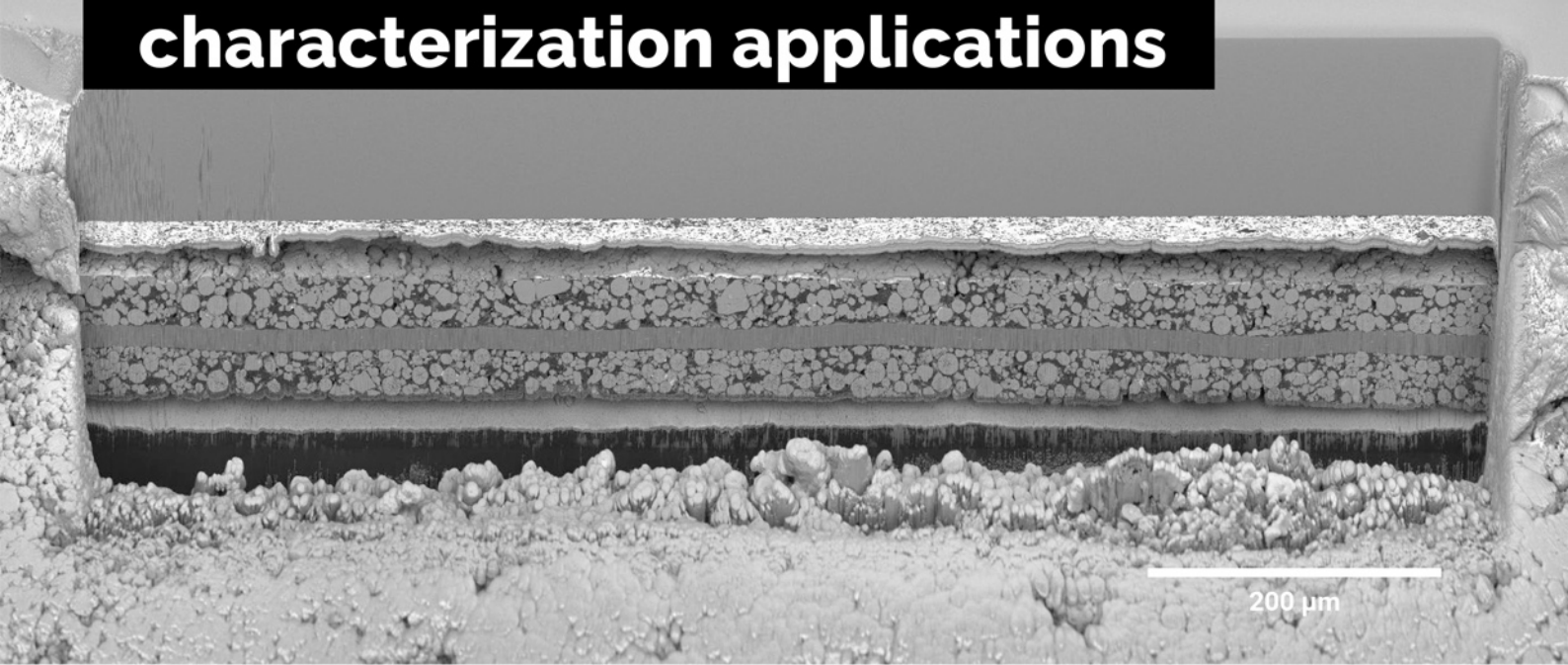


A unique combination of Plasma FIB and field-free UHR SEM for the widest range of multiscale materials characterization applications



1 mm cross-section through a Li-ion battery electrode

TESCAN AMBER X

- ✓ High throughput, large area FIB milling up to 1 mm
- ✓ Ga-free microsample preparation
- ✓ Ultra-high resolution, field-free FE-SEM imaging and analysis
- ✓ In-column SE and BSE detection
- ✓ Spot optimization for high-throughput, multi-modal FIB-SEM tomography
- ✓ Superior field of view for easy navigation
- ✓ Essence™ easy-to-use, modular graphical user interface



For more information visit

www.tescan.com

High-Entropy Sulfides as Electrode Materials for Li-Ion Batteries

Ling Lin, Kai Wang, Abhishek Sarkar, Christian Njé, Guruprakash Karkera, Qingsong Wang, Raheleh Azmi, Maximilian Fichtner, Horst Hahn, Simon Schweidler,* and Ben Breitung*

High-entropy sulfides (HESs) containing 5 equiatomic transition metals (M), with different M:S ratios, are prepared by a facile one-step mechanochemical approach. Two new types of single-phase HESs with pyrite (*Pa-3*) and orthorhombic (*Pnma*) structures are obtained and demonstrate a homogeneously mixed solid solution. The straightforward synthesis method can easily tune the desired metal to sulfur ratio for HESs with different stoichiometries, by utilizing the respective metal sulfides, even pure metals, and sulfur as precursor chemicals. The structural details and solid solution nature of HESs are studied by X-ray diffraction, transmission electron microscopy, energy-dispersive X-ray spectroscopy, electron energy loss spectroscopy, X-ray photoelectron spectroscopy, inductively coupled plasma optical emission spectroscopy, and Mössbauer spectroscopy. Since transition metal sulfides are a very versatile material class, here the application of HESs is presented as electrode materials for reversible electrochemical energy storage, in which the HESs show high specific capacities and excellent rate capabilities in secondary Li-ion batteries.

1. Introduction

In recent years, a novel material class, the high-entropy materials (HEMs), has developed very rapidly and is gaining popularity. Specifically, the high-entropy concept aims to introduce a large number of different elements into a single-phase lattice, which does not only leads to high configurational entropy, but also creates a unique combination of interactions based on the stoichiometry and type of incorporated elements. The high-entropy concept was first applied to alloy systems^[1–3] and later deployed at ceramics including oxides,^[4,5] oxyfluorides,^[6,7] silicides,^[8] borides,^[9] nitrides,^[10] carbides,^[11,12] chalcogenides,^[13–16] fluorides,^[17–19] phosphides,^[20,21] etc. Yeh summarized four core factors affecting the microstructure and properties of high-entropy alloys:^[22] configurational entropy, sluggish diffusion, lattice distortion, and cocktail effects, all of which can be trans-

ferred to high-entropy ceramics (HECs) as well. The strongest impact on the material properties arises from the elemental composition of the HEMs and can be described with the so-called cocktail effect, which outlines the materials' properties in terms of the elemental interactions. By changing the stoichiometry or the type of the incorporated elements, the material can be tailored regarding certain desired properties. Additionally, lattice distortions due to differently sized ions are apparent, which can also alter the mechanical and physical properties of a material. All of the above enable HEMs to show exciting and unexpected properties with a broad range of applications, for example in catalysis,^[23,24] as thermoelectric material,^[15,25] and for electrochemical energy storage.^[4,6]

The configurational entropy is an important value for judging if the material is a high-entropy compound ($S_{\text{config}} > 1.5R$), which can be calculated by following a formula (Equation (1)) derived from the Boltzmann and Gibbs interpretation of entropy.^[5,26]

$$S_{\text{config}} = -R \left[\left(\sum_{i=1}^N x_i \ln x_i \right)_{\text{sl1}} + \left(\sum_{j=1}^M x_j \ln x_j \right)_{\text{sl2}} \right] \quad (1)$$

In this equation, S_{config} describes the configurational entropy, R is the ideal gas constant, and sl1 and sl2 stand for different sub-lattices in the structure. x_i and x_j represent the molar fraction of the i_{th} and j_{th} component of the respective sublattice,


L. Lin, K. Wang, A. Sarkar, Q. Wang, H. Hahn, S. Schweidler, B. Breitung
Institute of Nanotechnology
Karlsruhe Institute of Technology (KIT)
Hermann-von-Helmholtz-Platz 1, 76344 Eggenstein-Leopoldshafen, Germany
E-mail: simon.schweidler@kit.edu; ben.breitung@kit.edu

A. Sarkar, H. Hahn
Joint Research Laboratory Nanomaterials
Technische Universität Darmstadt and Karlsruhe Institute of Technology
Otto-Berndt-Str. 3, 64206 Darmstadt, Germany

C. Njé, R. Azmi
Institute for Applied Materials (IAM) and
Karlsruhe Nano Micro Facility (KNMF)
Karlsruhe Institute of Technology (KIT) Hermann-von-Helmholtz-Platz 1
76344 Eggenstein-Leopoldshafen, Germany

G. Karkera, M. Fichtner
Helmholtz Institute Ulm
Helmholtzstr. 11, 89081 Ulm, Germany

Q. Wang
INM – Leibniz Institute for New Materials
Campus D2 2, 66123 Saarbrücken, Germany

 The ORCID identification number(s) for the author(s) of this article can be found under <https://doi.org/10.1002/aenm.202103090>.

© 2022 The Authors. Advanced Energy Materials published by Wiley-VCH GmbH. This is an open access article under the terms of the Creative Commons Attribution-NonCommercial License, which permits use, distribution and reproduction in any medium, provided the original work is properly cited and is not used for commercial purposes.

DOI: 10.1002/aenm.202103090

N and M are corresponding to the number of elements in the sub-lattices, respectively.

HESs constitute a HEM class that was only discovered very recently. In 2018,^[15] Zhang et al. synthesized tetragonally structured (*I-42m*), multi-component sulfides $\text{Cu}_5\text{SnMgGeZnS}_9$ and $\text{Cu}_3\text{SnMgInZnS}_7$ by mechanical alloying and spark plasma sintering for thermoelectric applications ($1R < S_{\text{config}} < 1.5R$, a medium-entropy material). In 2020,^[14] Cui et al. reported on a high-entropy cubic (*Fm-3m*) $(\text{CrMnFeCoNi})_9\text{S}_8$ as catalyst for oxygen evolution reaction, synthesized by a pulse thermal decomposition method and later, in 2021,^[13] McCormick et al. introduced a simultaneous multication exchange pathway to get the wurtzite-type HES $\text{Zn}_{0.25}\text{Co}_{0.22}\text{Cu}_{0.28}\text{In}_{0.16}\text{Ga}_{0.11}\text{S}$. The field of HESs is still in its infancy, but already the few publications demonstrate that the structure and properties of these materials are rather unique.

Conventional transition metal sulfides (TMSs), as an important class of inorganics, possess electrical, mechanical, magnetic, and optical properties and have been widely studied in the field of catalysis,^[27] photonics,^[28] electrochemistry,^[29] tribology,^[30] and magnetism.^[31] For electrochemical energy storage in Li-ion batteries, Na-ion batteries, and supercapacitors, TMSs have attracted great attention as outstanding electrode candidates due to their high theoretical specific capacities and low-cost.^[29,32] For example, cobalt sulfides (CoS_x) are promising conversion type electrode materials due to their large theoretical specific capacities (Co_9S_8 : 545 mAh g^{-1} , CoS : 589 mAh g^{-1} , Co_3S_4 : 702 mAh g^{-1} , CoS_2 : 870 mAh g^{-1}).^[32]

In this report, we present the synthesis and characterization of novel HESs, including pyrite (*Pa-3*) MS_2 (M being Fe, Co, Ni, Mn, Cu, Cr, and Ti) and orthorhombic (*Pnma*) MS (M being Fe, Co, Ni, Mn, and Cr), and for the first time apply HESs as electrode materials for battery applications. Through a facile one-step mechanochemical reaction, using metal sulfides and even elemental precursors (sulfur and metal), homogenous solid solution HESs with different metal to sulfur ratios can be easily obtained, which avoids complex procedures and high-temperature processes as necessary for many other preparation techniques.^[13–15] The new HESs were characterized comprehensively using X-ray diffraction (XRD), transmission electron microscopy (TEM), electron energy loss spectroscopy (EELS), energy-dispersive X-ray spectroscopy (EDX), X-ray photoelectron spectroscopy (XPS), inductively coupled plasma optical emission spectroscopy (ICP-OES) and Mössbauer spectroscopy. In Li-ion battery, it was found that HESs exhibit improved capacities compared to binary sulfides.^[32] The remarkable specific capacities and excellent rate capabilities demonstrate their applicability as conversion electrode materials for batteries, meanwhile our mechanochemical method provides a simple and general approach to multi-metal sulfides with tailored M:S ratios for various applications.

2. Results and Discussion

Herein, we report on the successful synthesis of HESs with different M:S ratios by a facile one-step high-energy ball-milling method at room temperature in inert argon atmosphere. As precursors, the respective concentrations of metal sulfides,

Table 1. Overview about the different prepared samples.

Composition	Structure	Abbreviation
$(\text{FeMnNiCoCr})_3\text{S}_2$	Multiphase: <i>Pnma</i> , <i>Fd-3m</i> , <i>P6_3mc</i>	M3S2
$(\text{FeMnNiTiCr})\text{S}$	Multiphase: <i>Pnma</i> , <i>Fd-3m</i> , <i>P6_3mc</i>	MS-Ti
$(\text{FeMnNiCoCr})\text{S}$	<i>Pnma</i>	MS
$(\text{FeMnNiCoCr})_3\text{S}_4$	Multiphase: <i>Pa-3</i> , <i>Pnma</i>	M3S4
$(\text{FeMnNiCoCr})_2\text{S}_3$	Multiphase: <i>Pa-3</i> , <i>Pnma</i>	M2S3
$(\text{FeMnNiCoCr})\text{S}_2$	<i>Pa-3</i>	MS2
$(\text{FeMnNiCoCu})\text{S}_2$	<i>Pa-3</i>	MS2-Cu
$(\text{FeMnNiTiCr})\text{S}_2$	<i>Pa-3</i>	MS2-Ti

metal and sulfur, based on the stoichiometry of the desired compound, were used. The different compositions, structures, and abbreviations can be found in **Table 1**. The high-entropy monosulfides $(\text{FeMnNiCoCr})\text{S}$ and $(\text{FeMnNiTiCr})\text{S}$ are marked as MS and MS-Ti, the prepared high-entropy disulfides $(\text{FeMnNiCoCr})\text{S}_2$, $(\text{FeMnNiTiCr})\text{S}_2$, and $(\text{FeMnNiCoCu})\text{S}_2$ are referred to MS2, MS2-Ti, and MS2-Cu, respectively. For comparison, other M:S ratios, that is, $(\text{FeMnNiCoCr})_2\text{S}_3$, $(\text{FeMnNiCoCr})_3\text{S}_4$, $(\text{FeMnNiCoCr})_3\text{S}_2$ (named as M2S3, M3S4, and M3S2, respectively) were also synthesized. Since all 5 cations are always introduced in equimolar proportions, the configurational entropy (S_{config}) of all these HESs amounts to 1.61R. These stoichiometries were chosen to find out about the possibility to prepare the high-entropy versions of the respective structures, examples for the individual stoichiometries are FeS (*Pnma*),^[33] FeS_2 (*Pa-3*),^[34] Cr_2S_3 (*R-3*),^[35] Ni_3S_4 (*Fd-3m*),^[36] and Ni_3S_2 (*R32*).^[37]

X-ray diffraction measurements were performed to determine the crystal structure and whether a single phase was present after synthesis. **Figure 1a** shows the comparison of the different XRD patterns, with two different structures formed for MS and MS2, as expected. Depending on the elemental composition, shifts of the reflection positions appear, originating from the different sizes of the incorporated elements (**Figure 1b**).

As can be noticed, two typical structures appear for all HESs, but some of the components contain multiple phases. The MS and MS2 compounds appear to be predominantly single-phase, while M3S2 and M3S4 clearly show a mixture of different structures. For binary materials, M3S2 only exists with Ni as transition metal cation: Ni_3S_2 -*R32* (ICDD PDF No. 00-044-1418), while for M3S4 the respective elements adopt many different structures: for example, Fe_3S_4 -*Fd-3m* (ICDD PDF No. 00-016-0713) and *R-3m* (ICDD PDF No. 01-089-2000), Ni_3S_4 -*Fd-3m* (ICDD PDF No. 00-047-1739), Cr_3S_4 -*I2/m* (ICDD PDF No. 00-011-0008). Therefore, the mixing enthalpy might be too high to obtain stable single-phase compounds at room temperature for the high-entropy versions of M3S2 and M3S4. The typically observed structures for the MS and MS2 materials are *Pnma* and *Pa-3*, respectively, as in the corresponding binary components.

The crystal structures of the different HES can be compared based on their M:S ratios. The material with the lowest sulfur content, and therefore with the highest M:S ratio, is the multiphase M3S2 material. With a decreasing M:S ratio, multiphase M3S2 transforms into a single-phase MS type structure with *Pnma* space group. As the relative sulfur content

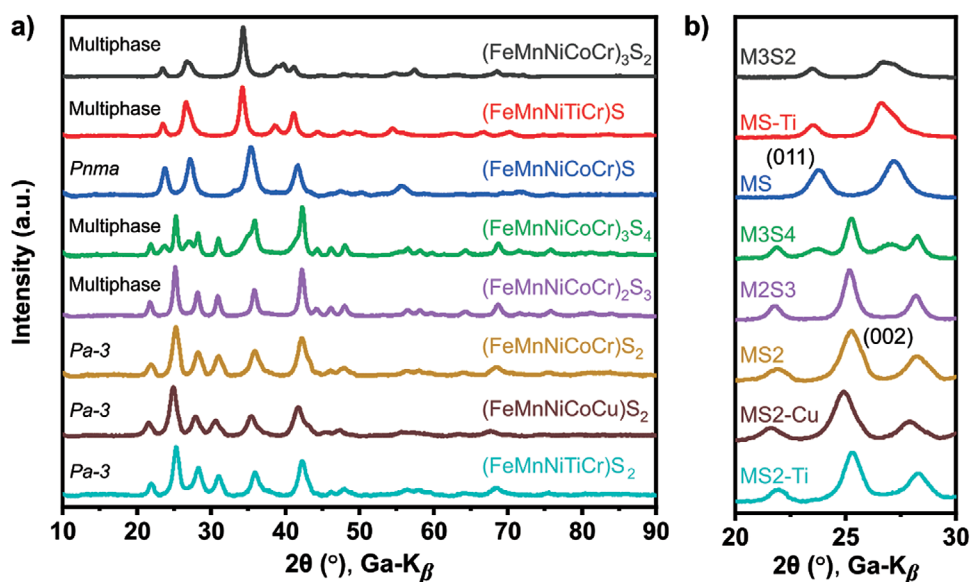


Figure 1. a) Comparison of XRD patterns of as-synthesized HESs with different M:S ratios and element composition. b) Transition of HESs structure from *Pnma* to *Pa-3* space group occurs with increasing sulfur content. Comparison of the (002) reflection position of pyrite sulfides. The shifts can be related to the different incorporated ions. The data is background corrected.

continues to rise, a pyrite phase (*Pa-3*) starts to appear and a material containing both phases is formed (M3S4). When the M:S ratio is further decreased, a pure pyrite structure appears. Note that the XRD pattern of M2S3 also shows an almost single-phase MS2 structure. This discrepancy between structure and stoichiometry can be explained by the formation of an inconspicuous MS phase, detectable in SAED measurements as explained later, which changes the M:S ratio towards an MS2 stoichiometry (M2S3–MS → MS2).

Substitution of certain transition metals was made to evaluate the stability of the compounds when smaller or larger ions are incorporated and precursors with different oxidation states were used. Previous studies have revealed that high-entropy systems are able to compensate charges by reducing or oxidizing other elements in the same lattice, therefore keeping the average charge of the original parent structure.^[38–40] MS-Ti is obtained by replacing Co of MS with Ti and therefore replacing Co^{2+} (0.745 Å) by Ti^{4+} (0.605 Å).^[41] However, the compound doesn't form a single phase, a phase mixture of *Pnma*, *Fm-3m*, and *P63mc* (Figure S1, Supporting Information) was found. Compared to the MS compounds, the MS2 structure is less affected by the $\text{Co} \rightarrow \text{Ti}$ replacement. Generally, MS2 compounds show different oxidation states of the sulfur anions compared to MS compounds. For example, in FeS_2 , Fe appears in a 2+ state and S as S_2^{2-} anion with S being –1, in analogy to the peroxide anion.^[34] The appearance of the disulfide anion (S_2^{2-}) also explains the different properties of disulfides, for example, in battery, as shown later. The divalent state of the metal ion in binary MS2 materials is also adopted by the other incorporated elements (except Ti^{4+} in TiS_2), therefore it is expected to find disulfide ions as well. Nevertheless, as shown later by XPS and EELS measurements, the anions in the high-entropy MS2 compounds are mixed, with some S^{2-} observed as anion, therefore we expect that M^{2+} and M^{4+} cations can be incorporated into the structure. Due to this circumstance, the replacement of Co^{2+}

with Ti^{4+} in MS2-Ti could be successfully executed without the formation of secondary phases. To further test the charge compensation mechanisms in the material, Cr, which can appear as 3+ and 6+ (0.62 and 0.44 Å) and was reported to be a strong mediating element in charge compensation mechanisms, was replaced by the much larger Cu^{2+} (0.73 Å) that cannot take higher oxidation states in MS2-Cu. Even though no charge compensation is possible and despite the large ionic size deviation, MS2-Cu could also be prepared as single-phase material. A strong indication that Ti^{4+} and Cu^{2+} are really incorporated into the lattice is obtained by the shift of the reflections in Figure 1b to larger or smaller angles, respectively. This shows the high flexibility and resilience of MS2 compounds for incorporation of different sized and charged ions. We assume that the synthesis process, using elemental sulfur among other species as precursor, allows the formation of S^{2-} and S_2^{2-} anions and therefore can adapt to the oxidation state of the metals. This was also demonstrated by the characterization of the newly prepared materials in the following.

The single-phase structures MS, MS2, MS2-Ti, and MS2-Cu were further investigated in more detail to find out about the lattice parameters and the impact of Ti^{4+} and Cu^{2+} substitution (Table 2). Refinement of the pattern (Figure 2a) indicates that MS shows a unit cell volume of $110.4(1) \text{ \AA}^3$ and the lattice parameters $a = 5.443(3) \text{ \AA}$, $b = 3.428(3) \text{ \AA}$, and $c = 5.913(5) \text{ \AA}$. Refinement of M3S4 confirms the presence of a *Pnma* and a *Pa-3* structure, which is a mixture of MS and MS2, as shown in Figure S2a, Supporting Information. Figure S2b, Supporting Information, shows that M2S3 is mainly a *Pa-3* structure. Compared to MS2 ($a = 5.618(1) \text{ \AA}$, $V = 177.3(1) \text{ \AA}^3$, Figure 2b), the incorporation of Cu in MS2-Cu expands the lattice and the length of the *a*-axis ($a = 5.666(4) \text{ \AA}$, $V = 181.8(4) \text{ \AA}^3$, Figure S2c, Supporting Information), the replacement of Co by Ti in MS2-Ti reduces the unit cell ($a = 5.611(3) \text{ \AA}$, $V = 176.7(3) \text{ \AA}^3$, Figure S2d, Supporting Information).

Table 2. Refined lattice parameters and unit cell volume of MS and different MS2 compounds.

Materials	Space group	<i>a</i> [Å]	<i>b</i> [Å]	<i>c</i> [Å]	<i>V</i> [Å ³]	χ^2	Phase density [g cm ⁻³]
MS	<i>Pnma</i>	5.443(3)	3.428(3)	5.913(5)	110.4(1)	2.9	5.168(3)
MS2	<i>Pa-3</i>	5.618(1)	/	/	177.3(1)	1.4	4.535(2)
MS2-Cu	<i>Pa-3</i>	5.666(4)	/	/	181.8(4)	1.3	4.735(9)
MS2-Ti	<i>Pa-3</i>	5.611(3)	/	/	176.7(3)	1.2	4.439(7)

The elemental composition of HESs was determined by ICP-OES (Table 3). The theoretical ratio of metal to sulfur (assuming MS, MS2) was almost achieved. All transition metals are nearly in an equimolar ratio, which validates the calculated configurational entropy of $S_{\text{config}} > 1.5R$ according to Equation (1). The EDX values are given in Table S3, Supporting Information. Compared to the ICP measurements, a slight stoichiometry change appears, which is in the range of accuracy.

TEM analysis was conducted to further investigate the structural details of the materials using MS and MS2 as examples. The morphology of HESs can be described as polycrystalline particles with sizes of \approx tens to hundreds of nanometers, as shown in Figure S3, Supporting Information. Figure 3a,b shows high-resolution TEM (HR-TEM) micrographs of MS and MS2. The yellow circled area corresponds to (011) diffraction plane in MS with lattice spacing of 0.30 nm, and red circled area refers to (002) lattice planes of the pyrite structure for MS2.

SAED was measured for MS, MS2, and M2S3 (Figure 3c,d and Figure S3, Supporting Information). For MS and MS2, the diffraction rings are consistent with the XRD measurements and are in agreement with *Pnma* and *Pa-3* space group, respectively (Table S1, Supporting Information). Figure S4,

Supporting Information, shows the SAED taken from M2S3. Beside the (022) diffraction ring of the main pyrite phase, some diffraction spots corresponding to 0.19 nm d-spacing appear, most probably corresponding to some multi cation MS crystallites or unreacted precursors (the most intense reflection of CoS, NiS, CrS, and FeS appears at a d-spacing of 0.19–0.20 nm) and would explain the formation of the pyrite phase for M2S3. The crystallites seem to be too small to be detected by XRD, therefore these diffraction signals only appear in SAED.

Figure 4 shows the elemental distribution of MS and MS2 as revealed by STEM-EDX elemental mapping. All elements are homogeneously distributed at the nanometer scale, without significant accumulation or segregation of individual elements. The uniform elemental distribution indicates the highest possible configurational entropy. High-resolution EDX mapping, confirming the homogenous distribution of the elements, is shown for MS and MS2 in Figures S5 and S6, Supporting Information, respectively.

In order to gather further information about the oxidation states of HESs with different M:S ratios, EELS and XPS were conducted to study the bulk and surface chemical state of MS and MS2 samples (Figures S7 and S8, Supporting Information).

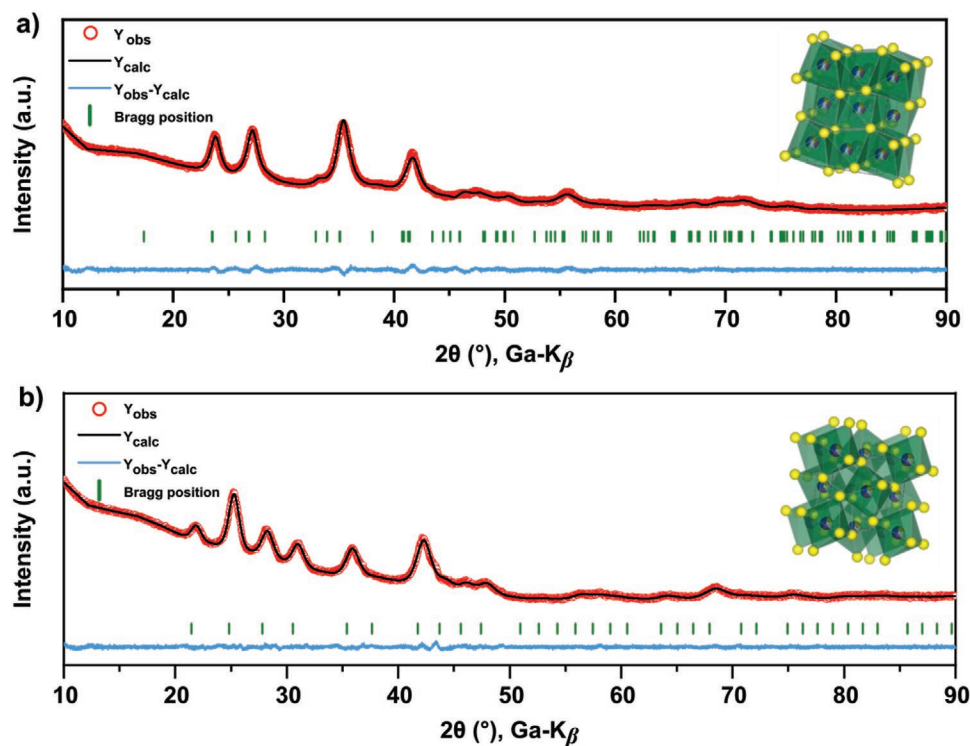


Figure 2. Rietveld refinement of a) MS: (FeMnNiCoCr)S and b) MS2: (FeMnNiCoCr)S₂.

Table 3. Stoichiometry of HESs from ICP-OES analysis.

Materials	Normalized to sulfur (exact)	Metal to sulfur ratio (exact)
MS	(Fe _{0.21} Mn _{0.21} Ni _{0.21} Co _{0.20} Cr _{0.21})S ₁	1.04:1 (=M ₁ S ₁ , <i>Pnma</i>)
MS2	(Fe _{0.11} Mn _{0.10} Ni _{0.10} Co _{0.10} Cr _{0.10})S ₁	0.51:1 (=M ₁ S ₂ , <i>Pa-3</i>)
MS2-Cu	(Fe _{0.11} Mn _{0.10} Ni _{0.11} Co _{0.10} Cu _{0.11})S ₁	0.53:1 (=M ₁ S ₂ , <i>Pa-3</i>)
MS2-Ti	(Fe _{0.10} Mn _{0.10} Ni _{0.09} Cr _{0.10} Ti _{0.09})S ₁	0.48:1 (=M ₁ S ₂ , <i>Pa-3</i>)

The samples seem to be slightly oxidized, forming SO_x compounds on the surface, which are detected by XPS. The oxidation state of the transition metal compounds is difficult to determine with high precision, therefore they should be seen as an indication for the average oxidation state. Additionally, in a compound with a random homogeneous distribution of transition metals, the characteristic energy can shift slightly due to different ionic environments. Without an exact reference, which does not exist due to the novelty of the compound, an exact determination of the oxidation state is nearly impossible. From XPS and EELS, the most probable oxidation state for the metals in MS and MS2 appears to be 2+, with an exception of Fe and Cr, which show different oxidation states (see Figure S7, Supporting Information, and corresponding EELS description in the Supporting Information).^[42–46] Since the majority of the cations are in a 2+ oxidation state, but there is some indication for 3+ as well, disulfides have to be present in the high-entropy MS2 besides the S²⁻ species.

Survey XPS spectra (Figure 5a) reveal the presence of eight main elements such as sulfur (S2p), carbon (C1s), oxygen (O1s), chromium (Cr2p), iron (Fe2p), manganese (Mn2p), cobalt (Co2p), and nickel (Ni2p). With the information depth of XPS analysis of about 5–10 nm, very surface-sensitive information of HESs (MS, M2S3, and MS2) polycrystalline particles are obtained. Figure 5b,c shows O1s and S2p of HESs with different M:S ratios (noted as MS, M2S3, and MS2).

The HESs seem to slightly react with oxygen under ambient conditions. The O1s spectra (Figure 5b) show signals from all oxygenated species present at the surface. The main peak at 531.8 eV can be attributed to a mixture of O=C, MOH (metal hydroxides), and oxygen from SO_x compounds. Another peak detected at a low binding energy (≈530.3 eV) indicates the presence of metal oxides (noted MO), which suggests an interaction of HESs with oxygen traces already present in glove box or the process of transferring to XPS analysis. All samples display one peak at a high binding energy (≈533.5 eV) attributed to a C–O environment. The S2p spectra have been fitted with 2p_{3/2}-2p_{1/2} doublets separated by 1.2 eV with 2/1 intensity ratio due to spin-orbit coupling. The S2p spectra show four components: I) the main doublet with 2p_{3/2} component at 161.7 eV (S1) is the signal of S²⁻ sulfur ion from MS structure. II) M2S3 and MS2 samples show the main doublet with 2p_{3/2} component at 162.9 eV (S2), corresponding to a S₂²⁻ (disulfide ion) environment, that can be always observed for M2S3 and MS2.^[47,48] (III+IV) in all HESs, two additional doublets with 2p_{3/2} at 167.4 (S4) and 164.2 eV (S3), corresponding to SO_x and S–S environments, respectively, could be found.

According to the literature, the spectra of the transition metals (Ni2p, Co2p, and Mn3s) reveal a 2+ oxidation state (Figure S8a–S8c, Supporting Information), which could correspond to a mixture of metal oxides and sulfides.^[49–51] The chromium spectra (Figure S8d, Supporting Information) show a chromium metal signal (at ≈574 eV) that is most likely due to chromium metal precursor. The presence of the two peaks at high binding energies (at ≈576 and ≈577 eV) suggests the partial oxidation of chromium, confirming the presence of a mixture of chromium sulfides and oxides, respectively, on the surface of the HESs samples.^[49]

Further, Mössbauer spectroscopy was performed to identify the chemical environments and electronic states of Fe in MS,

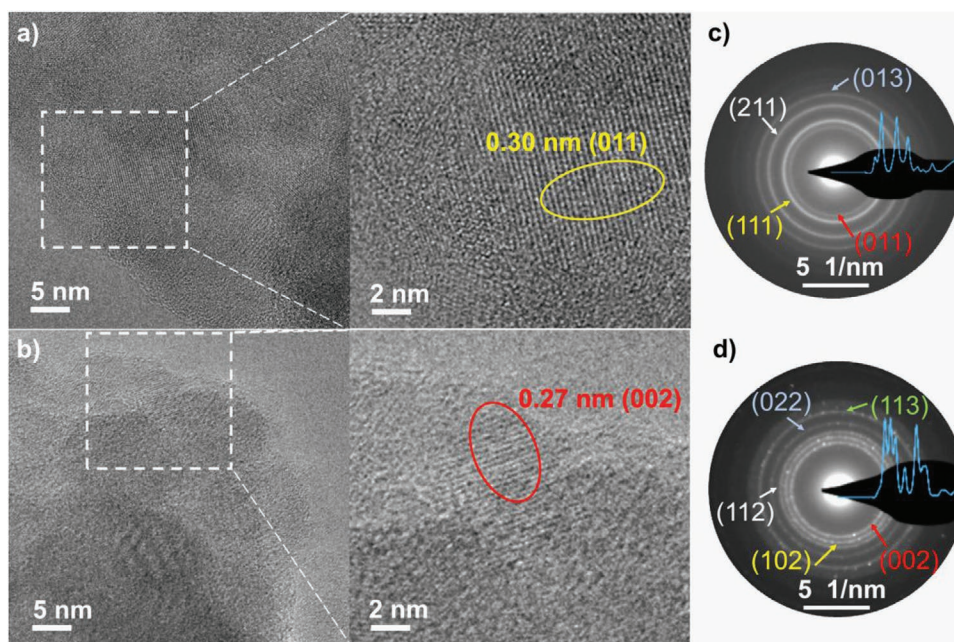


Figure 3. HR-TEM image with crystal lattices of a) MS and b) MS2. SAED patterns of c) MS and d) MS2.

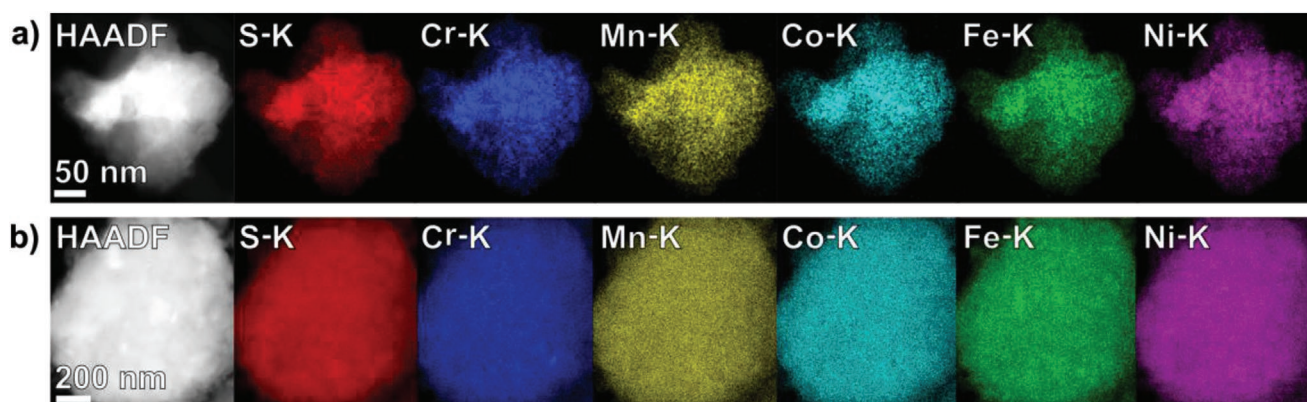


Figure 4. STEM-EDX mapping of a) MS and b) MS2. All elements are distributed uniformly.

MS2, and M2S3. This technique can distinguish extremely small changes in the chemical environment and oxidation state of Fe, resulting in splitting or shift of the peaks in the Mössbauer spectrum. Since the Mössbauer data could be fitted without any additional approximations, we assume that all Fe ions in the high-entropy structure have a very similar chemical environment, which means a statistical distribution without agglomerations or segregation of elements. Since a short-range order or changed chemical environments would change the response of the Fe ion, changes of the peak would appear, resulting in the necessity of additional subspectra in order to fit the whole spectrum.

Figure 6a shows the Mössbauer spectrum of MS, fitted by only one doublet, which corresponds to Fe^{2+} . The isomer shift (IS) of $0.598(4) \text{ mm s}^{-1}$ and the quadrupole split (QS) of

$0.691(7) \text{ mm s}^{-1}$, indicate a very uniform chemical environment of Fe in MS. Mössbauer data of MS2 (Figure 6b) are fitted by two quadrupole doublets sub-spectra, displaying two Fe^{3+} environments (doublet I and II) with different IS ($I = 0.350(7) \text{ mm s}^{-1}$, $II = 0.454(4) \text{ mm s}^{-1}$) and QS ($I = 0.527(9) \text{ mm s}^{-1}$, $II = 0.408(3) \text{ mm s}^{-1}$). Based on the quantification from the relative area fraction, Fe^{3+} (doublet I) accounts for the majority (90%) and Fe^{3+} (doublet II) accounts for 10% of the detected Fe^{3+} species. This can be an effect of the slightly oxidized surface, as also found in XPS measurements. Figure S9, Supporting Information, demonstrates that M2S3 also shows two different Fe environments, but not identical to MS2. Two quadrupole doublets sub-spectra from Fe in two oxidation states could be fitted to the MS2 spectra. 92% Fe show valence of +3, which is homogeneously distributed in pyrite HES.

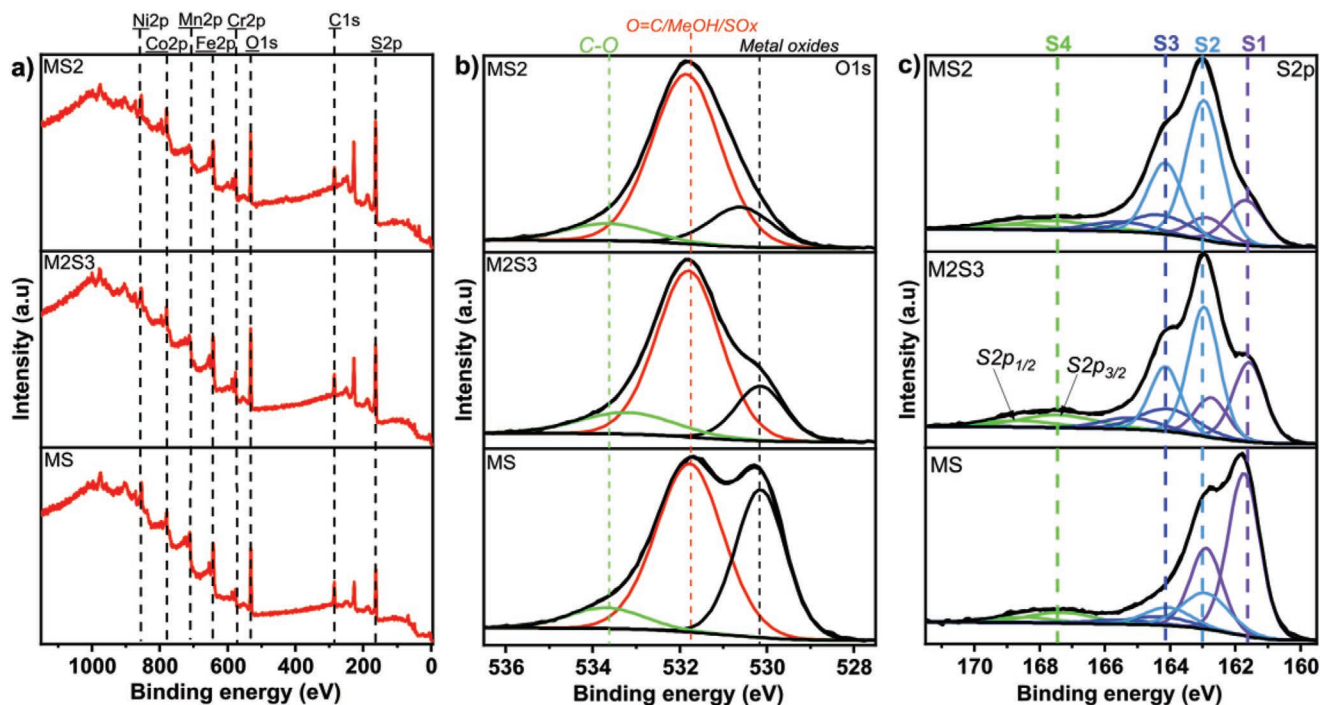


Figure 5. a) Survey, b) O1s, and c) S2p XPS spectra of HESs samples with different M:S ratios (MS, M2S3, and MS2 respectively).

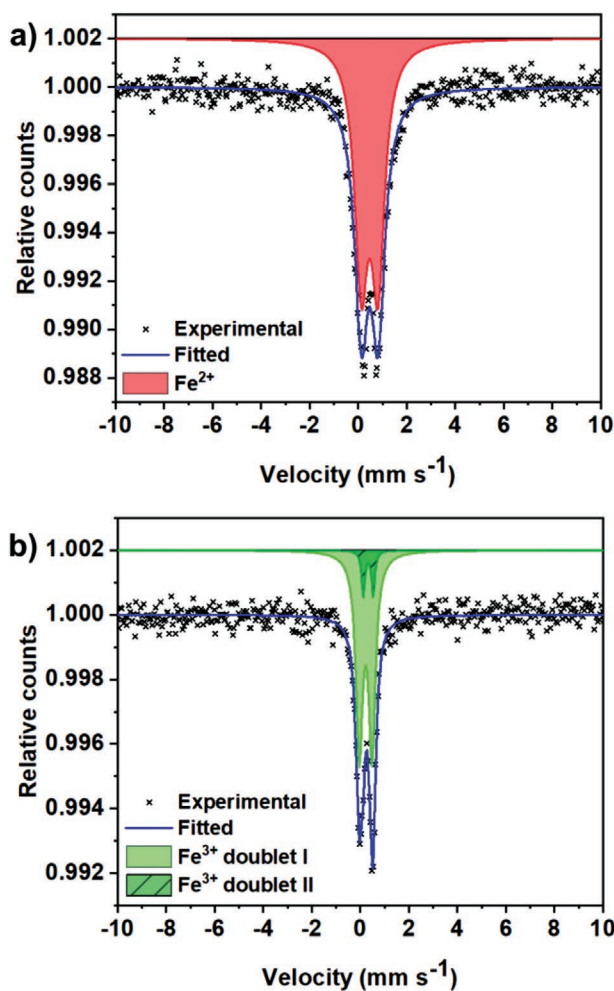


Figure 6. Mössbauer spectra of a) MS and b) MS2.

It displays a QS of $0.456(4) \text{ mm s}^{-1}$ and a nearly identical IS ($0.365(0) \text{ mm s}^{-1}$) compared to the Fe^{3+} (doublet I) in pure MS2. The remaining 8% is Fe^{2+} with doublet sub-spectrum of IS ($1.468(4) \text{ mm s}^{-1}$) and QS ($0.465(6) \text{ mm s}^{-1}$), corresponding to minor impure phase of mixed metal mono-sulfides which is also detected by SAED. This finding supports the assumption of an MS secondary phase, as already explained.

Finally, the HESs were investigated regarding their electrochemical properties. For this purpose, the HESs were mixed with multi-walled carbon nanotubes (MWCNTs) in a weight ratio of 9:1 (HES:MWCNTs) to increase the electronic conductivity. The HESs mixed with MWCNTs were used as active materials in half-cells with a lithium metal anode. The exact production of the slurry/tapes can be found in the experimental section. CoS_2 mixed with the same ratio of MWCNTs and pure MWCNTs were used as reference. Note, that some sulfides are sensitive against humidity and can degrade.^[52,53] Since the electrodes were prepared using aqueous binder, XRD measurements of the dried electrode were conducted to find out about potential decomposition of the material (Figure S10, Supporting Information). No decomposition products or changes in the structure could be observed, therefore it is expected that the HESs do not change during electrode preparation. XRD

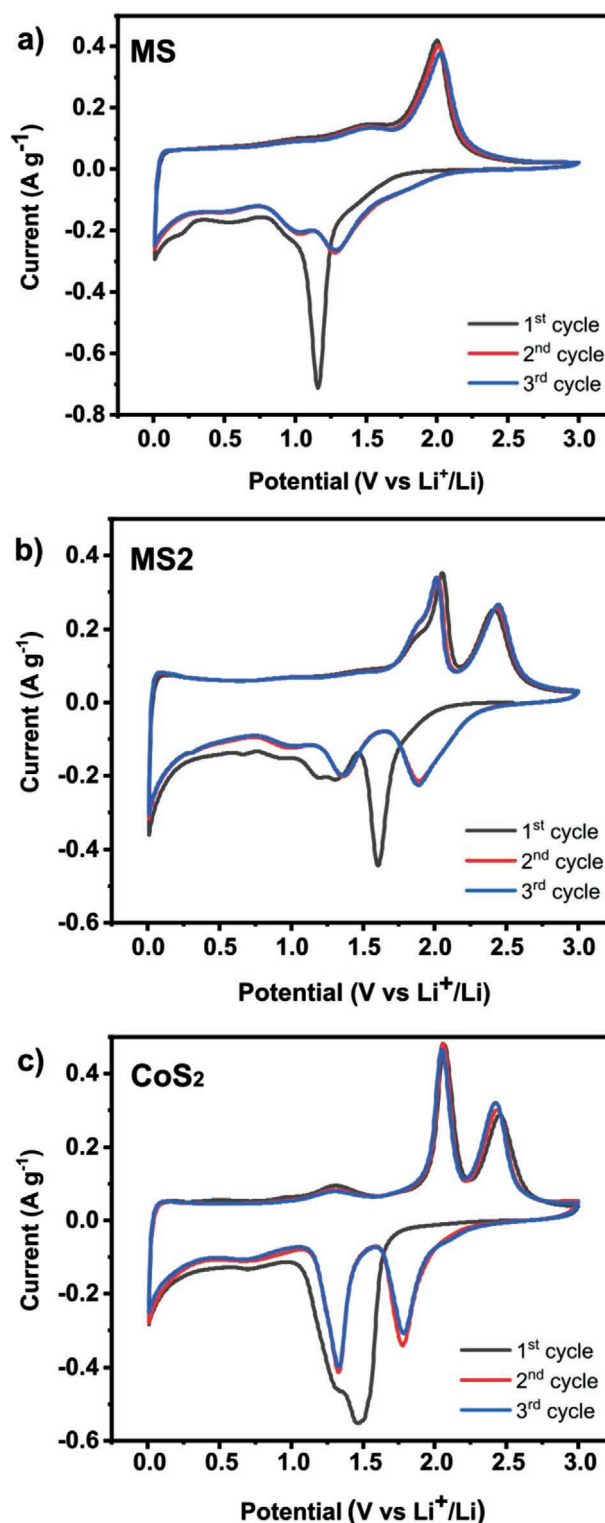


Figure 7. CV profiles of a) MS, b) MS2, and c) CoS_2 measured in the voltage range of 0.01–3 V versus Li^+/Li with a scan speed of 0.1 mV s^{-1} .

pattern of the electrodes prepared of the other compounds, can be found in Figure S11, Supporting Information.

Cyclic voltammetry (CV) was performed to investigate the electrochemical redox reaction potentials, as shown in Figure 7

and Figure S12, Supporting Information. In the initial lithiation process of MS₂, MS₂-Cu, and MS₂-Ti, the cathodic peaks between 0.8 to 1.7 V can be ascribed to the reduction of HESs to metal and Li₂S.^[54] Referring to the reaction of pyrite metal sulfides (such as FeS₂ and CoS₂), the first discharge reaction can be explained in two steps:^[32,55,56] 1) MS₂+xLi⁺+xe⁻ → Li_xMS₂ (peak at about 1.6 V), 2) Li_xMS₂+ (4-x)Li⁺+ (4-x)e⁻ → 2Li₂S+M. For the subsequent delithiation process, two distinct anodic peaks occur around 2.0 and 2.4 V, which can be assigned to two-step re-sulfidation process. The split of the anodic peak might be subject to the different sulfidation potentials of the incorporated transition metals.^[54,57] For the following cycles, in addition to the upshift of the reduction peaks to around 1.9 and 1.3–1.4 V, the CV curves almost overlap, indicating reversibility during the first cycles. While a significant shift of the reduction peaks can be observed between the CVs of MS₂ and CoS₂, the

oxidation peak does not change much (2.05 V vs 2.01 V vs Li⁺/Li). The reason for this behavior could not be detected at this stage of research and needs more detailed investigation on the reaction mechanism.

The redox performances in CV of pyrite-structure HESs are close to CoS₂ (Figure 7c), but show broader peaks and shifted reaction potentials, which could be due to the cocktail effect of multiple elements in HESs. In the first cycle of high-entropy mono-sulfides MS, there is one strong oxidation peak at about 2.0 V and no peak at 2.4 V, indicating single-step oxidation.

The peaks below 0.7 V of all HESs may be attributed to the Li-ion intercalation/insertion into the carbon materials (including MWCNTs and conductive additive), which is consistent with MWCNTs electrode in Figure S12c, Supporting Information.

The galvanostatic rate capability performance of the different HESs, CoS₂, and pure MWCNTs at different currents is given in

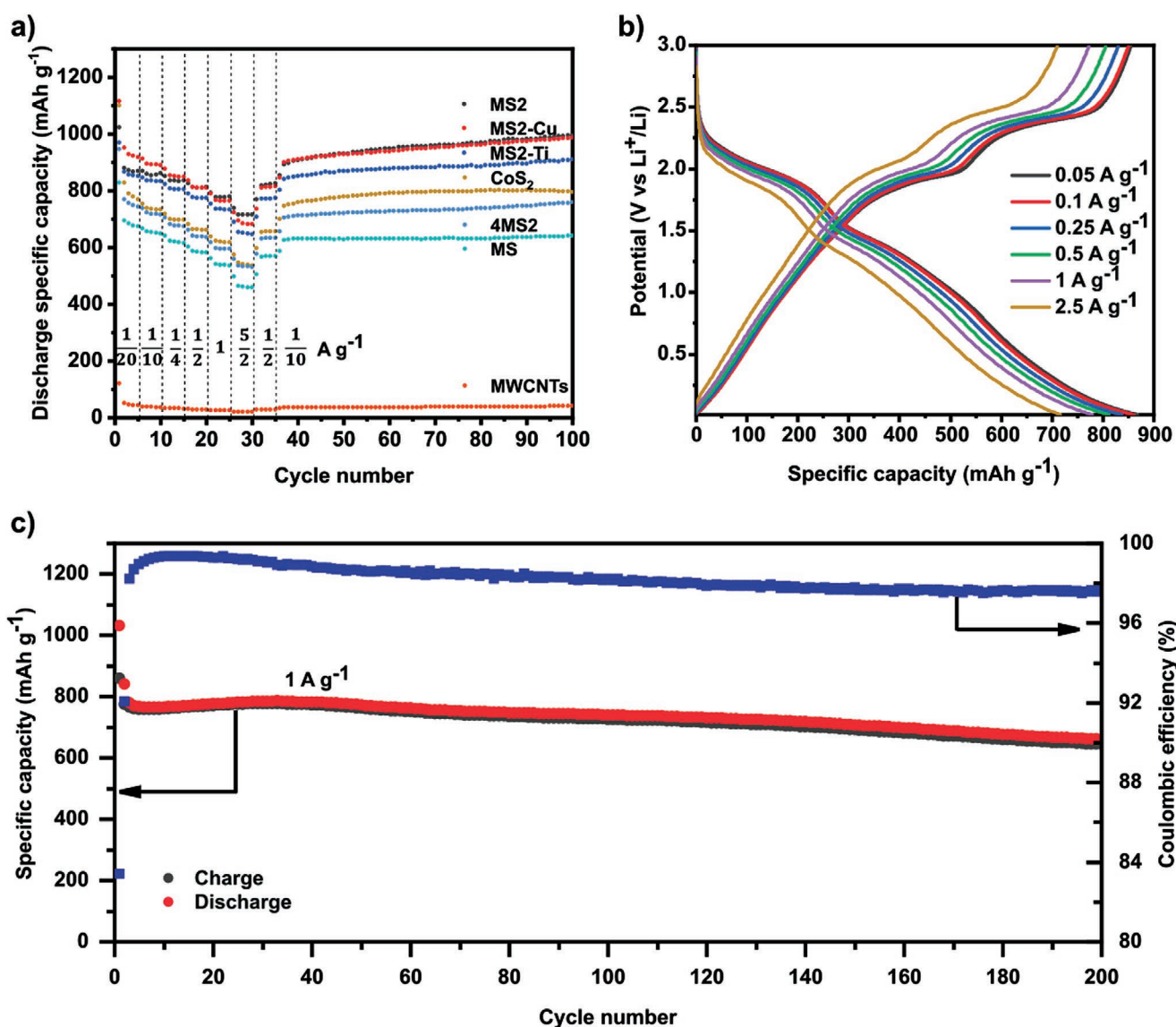


Figure 8. a) Galvanostatic rate performance test of all HESs, CoS₂, 4MS₂, and MWCNTs half-cell at different current densities and 25 °C in the voltage range between 0.01 and 3 V versus Li⁺/Li. b) Voltage profiles of MS₂ half-cell at different currents. c) Specific charge/discharge capacity of MS₂ half-cell and Coulombic efficiency as a function of cycle number at 1 C and 25 °C in the range between 0.01 and 3 V.

Table 4. Theoretical capacities of the high-entropy compounds.

Composition	Theoretical gravimetric capacity
MS	595 mAh g ⁻¹
MS2	885 mAh g ⁻¹
MS2-Cu	850 mAh g ⁻¹
MS2-Ti	927 mAh g ⁻¹

Figure 8a. The capacity shown for MWCNTs shown in Figure 8a, refers to the maximum capacity contribution of MWCNTs when mixed with HESs in a 1:9 ratio as executed for the electrodes. During the rate performance test, the MS2 materials show improved discharge capacities after 100 cycles (994, 909, and 986 mAh g⁻¹ for MS2, MS2-Ti, and MS2-Cu, respectively) compared to CoS₂ (795 mAh g⁻¹) and MS (642 mAh g⁻¹).

The theoretical capacities of the different compounds, calculated on the measured stoichiometry (ICP), are given in **Table 4**.

It can be seen that at low C-rates the received capacity seems to be larger than the theoretical capacity. The additional capacity, stems from the reaction of MWCNTs with Li at lower potentials and varies also with the respective C-rates (40–50 mAh g⁻¹). Note that this value has to be subtracted from the shown sulfide capacities in order to achieve the capacity solely derived from these compounds. In addition, conversion reactions often show slightly larger capacities than expected due to SEI formation, cracking of particles, irreversible reactions, etc. These reactions are often characterized by low Coulomb efficiencies, indicating irreversible capacity reactions (see Figure S13, Supporting Information). The increasing capacity in Figure 8a), starting from cycle 35, can be a result of the slow C-rate, which often leads to a combination of large volume expansions and SEI re/formation. This phenomenon cannot be observed anymore at higher C-rates (Figure 8c), since some slow reactions appearing during the conversion process are suppressed, reducing the reversible and irreversible capacity.

MS2-Cu initially exhibited the highest specific discharge capacities, however, with increasing current density (1 and 2.5 A g⁻¹), MS2 outperforms MS2-Cu. After returning to 0.5 and 0.1 A g⁻¹, MS2 and MS2-Cu again showed comparable values. In general, the HESs show good rate stability and long-term stability over the first 100 cycles (Figure 8a). Additionally, it is noticeable that the specific capacities also increase by approx. 200–300 mAh g⁻¹ as the absolute S fraction increases. This is due to the fact that metal disulfides can exchange more electrons and lithium ions in the conversion reaction than monosulfide materials, since it proceeds via a two-step reaction as explained earlier. Since MS2 showed the best performance (rate test), it will be discussed in more detail below. Figure 8b shows the voltage profiles of MS2 half-cells at different currents. From the voltage profiles at different currents, MS2 shows an excellent performance with reversible discharge capacities of 868, 860, 837, 812, 779, and 716 mAh g⁻¹ at current rate of 0.05, 0.1, 0.25, 0.5, 1, and 2.5 A g⁻¹, respectively. The plateaus at about 1.9 and 2.4 V seen in Figure 8b could also be an indication of the two-stage conversion process already mentioned above. Fong et al. observed a similar behavior for FeS₂.^[55] Moreover, the MS2 electrode shows good long-term stability. Even after 200 cycles at 1 A g⁻¹ and 25 °C, the MS2 half-cell provides a

specific capacity of 600 mAh g⁻¹ as well as high Coulombic efficiency of ≈98% (Figure 8c).

To demonstrate the positive influence of the high-entropy concept, the results were compared with a 4-component system (FeMnNiCo)S₂. Using only 4 different elements, a medium-entropy material is formed as the configurational entropy is decreased to <1.5R. The synthesis was done in the same way as for the high-entropy materials. From the electrochemical performance tests, the high-entropy materials show larger specific capacities than 4MS2 and the binary CoS₂.

Analysis of cycled electrodes confirmed several different lithiated sulfide species, depending on the state of charge of the analyzed electrode. A degradation of the material, eventually resulting in deposited S, could not be detected with XRD and EDX (Figures S14–S17, Supporting Information).

In general, this study shows the synthesis, characterization, and application of a new type of high-entropy materials, the high-entropy sulfides (HESs). Following up on the history of TMSs, which were investigated already in the late 70-s as active material for lithium batteries, the question can be brought up, if HESs might address the issues that lead to the fact that many ideas in this direction were dismissed.^[58] (The fundamental problems were the low cell potential and the lithium dendrite formation at the lithium anode. Since then, many years have passed and although the high-entropy concept at the cathode side will not influence the lithium dendrite formation at the anode, several protecting measures of the anode could be found and applied.^[59] The low potential of sulfide anodes on the other side might be an interesting field for follow-up investigations. With the introduction of the high-entropy concept, the introduction of metals into a certain structure is possible, which would not form this type of structure as binary sulfides (e.g., Cr in MS₂, CrS₂ cannot be prepared easily). Additionally, the high-entropy concept allows tailoring the materials composition in a way that elements can be replaced or added as shown in the previous work. Therefore, HESs with elements in unusual oxidation states or chemical environments are imaginable, which might show improved electrochemical performance. In summary, it might be worth revisiting the field of TMS cathodes for lithium-ion batteries, taking into account that anode protecting measures and tailorable materials that increase the number of possible materials into uncountable combinations, are now available.

3. Conclusion

In summary, this paper presents the preparation, characterization, and application of transition-metal-based HESs. The low-cost mechanochemical synthesis route avoids high-temperature preparation or solution processes and leads to (FeMnNiCoCr)S, (FeMnNiCoCr)S₂, (FeMnNiTiCr)S₂, and (FeMnNiCoCu)S₂ with expected M:S ratios. Novel single-phase HESs are formed in *Pnma* and *Pa-3* structures with uniformly distributed metals (Fe, Mn, Ni, Co, Cu, Cr, and Ti). Sulfur was found to appear as disulfide (S₂²⁻) and sulfide (S²⁻) anion. The HESs were tested as conversion active materials for Li-ion batteries in comparison with binary sulfides like CoS₂. It was found that the high-entropy MS2 compounds outperform the binary CoS₂, which

is an indication of the beneficial impact of the cocktail effects. This paper offers a pathway toward the design and synthesis of novel classes of high-entropy materials and countless further compositions for various applications.

4. Experimental Section

Synthesis: All chemicals were purchased from commercial sources (Sigma Aldrich/Alfa Aesar, Purity \geq 99%) and used without further purification. For the synthesis of all MS₂s, metal sulfides powders (FeS₂, CuS, MnS, Ni₃S₂, CoS₂, and TiS₂), Cr metal powder, and sulfur powder were ball-milled over 110 h in the respective metal to sulfur ratios. For the synthesis of MS, MS-Ti, M₂S₃, and M₃S₄, corresponding metal sulfides (FeS, MnS, Ni₃S₂, CoS₂, and TiS₂), Cr powder, and sulfur powder were ball-milled for 60 h in the respective metal to sulfur ratios. For the synthesis of M₃S₂, metal sulfides (FeS, MnS, and Ni₃S₂), Cr, Co, and sulfur powder were ball-milled for 60 h in the respective metal to sulfur ratios. All HESs were ball-milled at 500 rpm in high-purity argon atmosphere using a high-energy planetary ball-mill (Retsch PM 100, Retsch GmbH). 50 mL WC vials and 5 mm diameter WC balls were used. The weight ratio of balls to materials was 40:1.

Characterization: The elemental concentration of the as-prepared samples was determined by ICP-OES. The samples were dissolved in aqua regia (HCl: HNO₃, 3:1) and analyzed by performing a double determination using an ARCOS ICP-OES (Spectro Analytical Instruments, Kleve, Germany) with axial plasma view. Thermo Scientific K-alpha spectrometer was used to acquire the XPS spectra. The monochromatic AlK α line was used as X-ray excitation (1486.6 eV) with a pass energy of 50 eV to obtain high-resolution spectra. The samples were analyzed using a microfocused, monochromated Al K α X-ray source (400 μ m spot size). XPS spectra were fit with one or more Voigt profiles (binding energy uncertainty: \pm 0.2 eV) and Scofield sensitivity factors were applied for quantification.^[60] All spectra were referenced to the C1s peak (C–C, C–H) at 285.0 eV binding energy controlled by means of the photoelectron peaks of metallic Cu, Ag, and Au, respectively. PXRD was operated on powder samples at room temperature, using an STOE Stadi P diffractometer, equipped with a Ga-jet X-ray source (Ga-K β radiation, 1.2079 Å). Refinement of the XRD pattern was performed using TOPAS Academics V5 software. Si served as a calibration sample to determine the instrumental resolution. Background refinement was done using a linear interpolation function comprising 36 parameters. TEM measurements (SAED, HRTEM, STEM-EDX, and EELS) were performed on powder samples dispersed on a holey carbon-coated gold grid and loaded onto a Gatan 648 vacuum transfer holder. The STEM-EDX was acquired using a beam current of 200 pA. The step size in Figure 5a,b are 2.4 and 1.6 nm. TEM imaging data were collected using a double corrected Thermo Fisher Themis Z, equipped with HAADF-STEM detector, Super-X EDX detector, and Gatan Continuum 970 HighRes image filter. The microscope was operated at an accelerating voltage of 300 kV. ⁵⁷Fe Mössbauer spectroscopy data was gathered by using a spectrometer in transmission geometry with a moving source of ⁵⁷Co in an Rh matrix and a triangular velocity variation. The isomer shift was given relative to bcc-Fe measured at room temperature.

Electrochemistry: The active materials were obtained by ball-milling (6 h) with 10 wt.% MWCNTs and 90 wt.% HESs powder. The MWCNTs were purchased from commercial sources. (Sigma Aldrich, >7.5% MWCNT basis, outer diameter 7 to 15 nm, length 0.5 to 10 μ m). For electrode preparation, 70 wt.% active material, 10 wt.% Super C65 carbon black (Timcal), and 10 wt.% polyvinylidene fluoride (PVDF, Solef 5130, Solvay) in N-methyl-2-pyrrolidone were uniformly mixed to form a slurry and coated onto Cu foil. After dried in a vacuum oven at 80 °C overnight, circular electrodes (13 mm in diameter) were cut from the electrode tape with areal loading of active material around 0.5–1 mg cm⁻². All materials were tested in CR2032 type coin cells and assembled inside an Ar-filled glovebox. LP57 (1 M LiPF₆ in a 3:7 weight mixture of ethylene carbonate (EC)/ethyl methyl carbonate (EMC), BASF SE), GF/D glass microfiber filter

paper of diameter 17 mm (GE Healthcare Life Science, Whatman), and Li metal foil of diameter 13 mm (China Energy Lithium Co., Ltd) were used as the electrolyte, separator, and counter electrode, respectively. CV was performed on a Bio-logic VSP-300 potentiostat device at room temperature. The galvanostatic rate capability measurements were performed on an Arbin BT 2000 battery test system (Arbin Instruments) and LAND CT3001A battery test system (Wuhan LAND Electronic Co. Ltd) at 25 °C.

Supporting Information

Supporting Information is available from the Wiley Online Library or from the author.

Acknowledgements

L.L. acknowledges financial support from the China Scholarship Council (CSC). B.B. acknowledges the support from EnABLES and EPSTORE, projects funded by the European Union's Horizon 2020 research and innovation program under Grant Agreement Nos. 730957 and 101017709, respectively. A.S. and H.H. acknowledge financial support from the Deutsche Forschungsgemeinschaft (DFG) project HA 1344/43-2. The authors also thank KNMF (Karlsruhe Nano Micro Facility) and CELEST (Center for Electrochemical Energy Storage Ulm-Karlsruhe).

Open access funding enabled and organized by Projekt DEAL.

Conflict of Interest

The authors declare no conflict of interest.

Data Availability Statement

The data that support the findings of this study are available from the corresponding author upon reasonable request.

Keywords

high-entropy materials, high-entropy sulfides, lithium batteries, mechanochemical synthesis

Received: October 5, 2021

Revised: December 7, 2021

Published online: January 5, 2022

- [1] E. P. George, D. Raabe, R. O. Ritchie, *Nat. Rev. Mater.* **2019**, *4*, 515.
- [2] B. Cantor, I. T. H. Chang, P. Knight, A. J. B. Vincent, *Mater. Sci. Eng., A* **2004**, *375*, 213.
- [3] J. W. Yeh, S. K. Chen, S. J. Lin, J. Y. Gan, T. S. Chin, T. T. Shun, C. H. Tsau, S. Y. Chang, *Adv. Eng. Mater.* **2004**, *6*, 299.
- [4] C. Zhao, F. Ding, Y. Lu, L. Chen, Y.-S. Hu, *Angew. Chem., Int. Ed.* **2020**, *59*, 264.
- [5] C. M. Rost, E. Sachet, T. Borman, A. Moballegh, E. C. Dickey, D. Hou, J. L. Jones, S. Curtarolo, J. P. Maria, *Nat. Commun.* **2015**, *6*, 8485.
- [6] Z. Lun, B. Ouyang, D.-H. Kwon, Y. Ha, E. E. Foley, T.-Y. Huang, Z. Cai, H. Kim, M. Balasubramanian, Y. Sun, J. Huang, Y. Tian, H. Kim, B. D. McCloskey, W. Yang, R. J. Clément, H. Ji, G. Ceder, *Nat. Mater.* **2021**, *20*, 214.

- [7] Q. Wang, A. Sarkar, D. Wang, L. Velasco, R. Azmi, S. S. Bhattacharya, T. Bergfeldt, A. Düvel, P. Heitjans, T. Brezesinski, H. Hahn, B. Breitung, *Energy Environ. Sci.* **2019**, *12*, 2433.
- [8] Y. Qin, J.-X. Liu, F. Li, X. Wei, H. Wu, G.-J. Zhang, *J. Adv. Ceram.* **2019**, *8*, 148.
- [9] J. Gild, Y. Zhang, T. Harrington, S. Jiang, T. Hu, M. C. Quinn, W. M. Mellor, N. Zhou, K. Vecchio, J. Luo, *Sci. Rep.* **2016**, *6*, 37946.
- [10] T. Jin, X. Sang, R. R. Unocic, R. T. Kinch, X. Liu, J. Hu, H. Liu, S. Dai, *Adv. Mater.* **2018**, *30*, 1707512.
- [11] X. Yan, L. Constantin, Y. Lu, J. F. Silvain, M. Nastasi, B. Cui, *J. Am. Ceram. Soc.* **2018**, *101*, 4486.
- [12] P. Sarker, T. Harrington, C. Toher, C. Oses, M. Samiee, J. P. Maria, D. W. Brenner, K. S. Vecchio, S. Curtarolo, *Nat. Commun.* **2018**, *9*, 4980.
- [13] C. R. McCormick, R. E. Schaak, *J. Am. Chem. Soc.* **2021**, *143*, 1017.
- [14] M. Cui, C. Yang, B. Li, Q. Dong, M. Wu, S. Hwang, H. Xie, X. Wang, G. Wang, L. Hu, *Adv. Energy Mater.* **2021**, *11*, 2002887.
- [15] R. Z. Zhang, F. Gucci, H. Zhu, K. Chen, M. J. Reece, *Inorg. Chem.* **2018**, *57*, 13027.
- [16] Z. H. Deng, A. Olvera, J. Casamento, J. S. Lopez, L. Williams, R. Lu, G. S. Shi, P. F. P. Poudeu, E. Kioupakis, *Chem. Mater.* **2020**, *32*, 6070.
- [17] T. Wang, H. Chen, Z. Yang, J. Liang, S. Dai, *J. Am. Chem. Soc.* **2020**, *142*, 4550.
- [18] X. Chen, Y. Wu, *J. Am. Ceram. Soc.* **2020**, *103*, 750.
- [19] P. A. Sukkurji, Y. Cui, S. Lee, K. Wang, R. Azmi, A. Sarkar, S. Indris, S. S. Bhattacharya, R. Kruk, H. Hahn, Q. Wang, M. Botros, B. Breitung, *J. Mater. Chem. A* **2021**, *9*, 8998.
- [20] X. Zhao, Z. Xue, W. Chen, Y. Wang, T. Mu, *ChemSusChem* **2020**, *13*, 2038.
- [21] D. Lai, Q. Kang, F. Gao, Q. Lu, *J. Mater. Chem. A* **2021**, *9*, 17913.
- [22] J. W. Yeh, *JOM* **2013**, *65*, 1759.
- [23] S. H. Albedwawi, A. Aljaber, G. N. Haidemenopoulos, K. Polychronopoulou, *Mater. Des.* **2021**, *202*, 109534.
- [24] Y. Yao, Z. Huang, P. Xie, S. D. Lacey, R. J. Jacob, H. Xie, F. Chen, A. Nie, T. Pu, M. Rehwoldt, D. Yu, M. R. Zachariah, C. Wang, R. Shahbazian-Yassar, J. Li, L. Hu, *Science* **2018**, *359*, 1489.
- [25] S. Shafeie, S. Guo, Q. Hu, H. Fahlquist, P. Erhart, A. Palmqvist, *J. Appl. Phys.* **2015**, *118*, 184905.
- [26] B. S. Murty, J. W. Yeh, S. Ranganathan, *High-Entropy Alloys*, Butterworth-Heinemann, London **2014**.
- [27] J. Joo, T. Kim, J. Lee, S. I. Choi, K. Lee, *Adv. Mater.* **2019**, *31*, 1806682.
- [28] J. Yin, F. Zhu, J. Lai, H. Chen, M. Zhang, J. Zhang, J. Wang, T. He, B. Zhang, J. Yuan, P. Yan, S. Ruan, *Adv. Opt. Mater.* **2019**, *7*, 1801303.
- [29] P. B. Geng, S. S. Zheng, H. Tang, R. M. Zhu, L. Zhang, S. Cao, H. G. Xue, H. Pang, *Adv. Energy Mater.* **2018**, *8*, 1703259.
- [30] G. Chatzitheodorou, S. Fiechter, M. Kunst, J. Luck, H. Tributsch, *Mater. Res. Bull.* **1988**, *23*, 1261.
- [31] N. Sethulakshmi, A. Mishra, P. M. Ajayan, Y. Kawazoe, A. K. Roy, A. K. Singh, C. S. Tiwary, *Mater. Today* **2019**, *27*, 107.
- [32] J. Zhao, Y. Zhang, Y. Wang, H. Li, Y. Peng, *J. Energy Chem.* **2018**, *27*, 1536.
- [33] H. E. King, C. T. Prewitt, *Acta Crystallogr., Sect. B: Struct. Sci., Cryst. Eng. Mater.* **1982**, *38*, 1877.
- [34] A. P. Chandra, A. R. Gerson, *Geochim. Cosmochim. Acta* **2011**, *75*, 6239.
- [35] F. Jellinek, *Acta Crystallogr.* **1957**, *10*, 620.
- [36] Y. A. Kesler, S. G. Smirnov, K. V. Pokholok, B. N. Viting, *Inorg. Mater.* **1991**, *27*, 977.
- [37] P. A. Metcalf, P. Fanwick, Z. Kajokol, J. M. Honig, *J. Solid State Chem.* **1993**, *104*, 81.
- [38] Z. Rak, C. M. Rost, M. Lim, P. Sarker, C. Toher, S. Curtarolo, J. P. Maria, D. W. Brenner, *J. Appl. Phys.* **2016**, *120*, 095105.
- [39] D. Bérardan, S. Franger, D. Dragoë, A. K. Meena, N. Dragoë, *Phys. Status Solidi RRL* **2016**, *10*, 328.
- [40] N. Osenciat, D. Bérardan, D. Dragoë, B. Léridon, S. Holé, A. K. Meena, S. Franger, N. Dragoë, *J. Am. Ceram. Soc.* **2019**, *102*, 6156.
- [41] R. D. Shannon, *Acta Crystallogr., Sect. A: Found. Adv.* **1976**, *32*, 751.
- [42] T. L. Daulton, B. J. Little, *Ultramicroscopy* **2006**, *106*, 561.
- [43] T. Haiyan, J. Verbeeck, A. Abakumov, G. Van Tendeloo, *Ultramicroscopy* **2012**, *116*, 24.
- [44] P. A. van Aken, B. Liebscher, *Phys. Chem. Miner.* **2002**, *29*, 188;
- [45] J. L. Mansot, P. Leone, P. Euzen, P. Palvadeau, *Microsc. Microanal. Microstruct.* **1994**, *5*, 79.
- [46] F. Cosandey, D. Su, M. Sina, N. Pereira, G. G. Amatucci, *Micron* **2012**, *43*, 22.
- [47] L. Benoist, D. Gonbeau, G. Pfister-Guillouzo, E. Schmidt, G. Meunier, A. Levasseur, *Thin Solid Films* **1995**, *258*, 110.
- [48] D. Gonbeau, C. Guimon, G. Pfister-Guillouzo, A. Levasseur, G. Meunierand, R. Dormoy, *Surf. Sci.* **1991**, *254*, 81.
- [49] M. C. Biesinger, B. P. Payne, B. R. Hart, A. P. Grosvenor, N. S. McIntyre, L. W. Lau, R. S. Smart, *J. Phys.: Conf. Ser.* **2008**, *100*, 012025.
- [50] R. Azmi, V. Trouillet, M. Strafela, S. Ulrich, H. Ehrenberg, M. Bruns, *Surf. Interface Anal.* **2018**, *50*, 43.
- [51] J. L. Junta Jr., M. F. Hochella, *Geochim. Cosmochim. Acta* **1994**, *58*, 4985.
- [52] H. W. Nesbitt, M. Reinke, *Am. Mineral.* **1999**, *84*, 639.
- [53] C. N. R. Rao, K. P. R. Pisharody, *Prog. Solid State Chem.* **1976**, *10*, 207.
- [54] Y. Ma, Y. Ma, D. Bresser, Y. Ji, D. Geiger, U. Kaiser, C. Streb, A. Varzi, S. Passerini, *ACS Nano* **2018**, *12*, 7220.
- [55] R. Fong, J. R. Dahn, C. H. W. Jones, *J. Electrochem. Soc.* **1989**, *136*, 3206.
- [56] Q. H. Wang, L. F. Jiao, Y. Han, H. W. Du, W. X. Peng, Q. N. Huan, D. W. Song, Y. C. Si, Y. J. Wang, H. T. Yuan, *J. Phys. Chem. C* **2011**, *115*, 8300.
- [57] L. Liu, Z. Yuan, C. Qiu, J. Liu, *Solid State Ionics* **2013**, *241*, 25.
- [58] K. Brandt, *Solid State Ionics* **1994**, *69*, 173.
- [59] T. Wang, Y. Li, J. Zhang, K. Yan, P. Jaumaux, J. Yang, C. Wang, D. Shanmukaraj, B. Sun, M. Armand, Y. Cui, G. Wang, *Nat. Commun.* **2020**, *11*, 5429.
- [60] J. H. Scofield, *J. Electron Spectrosc. Relat. Phenom.* **1976**, *8*, 129.